

Comparing Reflection and Absorption Models for the Soft X-ray Variability in the NLS1 AGN UGC 11763

Jiachen Jiang,^{1*} Luigi C. Gallo,² Dirk Grupe,^{3,4} Michael L. Parker¹

¹*Institute of Astronomy, University of Cambridge, Madingley Road, Cambridge CB3 0HA, UK*

²*Department of Astronomy and Physics, Saint Mary's University, 923 Robie Street, Halifax, NS, B3H 3C3, Canada*

³*Department of Physics, Geology and Engineering Technology, Northern Kentucky University, Nunn Drive, Highland Heights, KY 41099, USA*

⁴*Department of Physics, Earth Science, and Space System Engineering, Morehead State University, 235 Martindale Dr, Morehead, KY 40351, USA*

Accepted XXX. Received YYY; in original form ZZZ

ABSTRACT

We present a spectral analysis of two *XMM-Newton* observations of the narrow-line Seyfert 1 galaxy UGC 11763. UGC 11763 shows very different soft X-ray spectral shapes in the two observations separated by 12 years. Three spectral models are considered to explain the multi-epoch X-ray variability of UGC 11763, one based on the relativistic disc reflection model, one based on multiple partially-covering absorbers combined with the warm corona model, and a hybrid model. In the first model, the X-ray variability of UGC 11763 is caused by the emission from a compact coronal region with a variable size. The resulting disc reflection component changes accordingly. A warm absorption model with a modest column density is required in this model too. In the partially-covering absorption scenario, the X-ray variability of UGC 11763 is caused by the variable covering factors of two absorbers located within a region of $r < \approx 100r_g$. Moreover, the temperature and strength of the warm corona have to change significantly too to explain the variable underlying soft X-ray emission. Lastly, we investigate the possibility of variable intrinsic power-law emission from the hot corona combined with variable absorption in UGC 11763 without changing the geometry of the corona in the third model. This hybrid model provides a slightly better fit than the partially-covering absorption model with improvements in fitting the iron emission band. Current CCD-resolution data cannot distinguish these spectral models for UGC 11763. Future high-resolution X-ray missions, e.g. *Athena* and *XRISM*, will test them by resolving different spectral components.

Key words: accretion, accretion discs - black hole physics, X-ray: galaxies, galaxies: Seyfert

1 INTRODUCTION

Narrow-line Seyfert 1 galaxies (NLS1s) are a class of peculiar Seyfert 1 galaxies (S1s) with strong Fe II emission, narrow H β emission and weak [O III] emission in the optical band in comparison with other S1s (Goodrich 1989). It is believed that NLS1s host low-mass supermassive black holes (BHs) that are accreting near or around the Eddington limit (e.g. Boroson 2002; Grupe & Mathur 2004), although some studies point out that the BH mass measurements of NLS1s might be biased towards low values when radiation pressure is ignored in the broad line region model for the H β emission of NLS1s (Marconi et al. 2008).

In the X-ray band, the nuclei of NLS1s often show rapid, large-amplitude X-ray variability (e.g. McHardy et al. 1995; Boller et al. 2003; Smith & Vaughan 2007; Jin et al. 2017; Alston et al. 2019) and steep X-ray continuum emission (Puchnarewicz et al. 1992; Boller et al. 1996; Grupe et al. 1998). Gallo (2006) finds that NLS1s

show complex spectral features in the X-ray band, especially during their low flux state. In particular, NLS1s often show strong excess emission below 2–3 keV in addition to the hard X-ray continuum extrapolated to the soft X-ray band (Boller et al. 1996; Piconcelli et al. 2005).

Different models have been proposed to explain the broad-band X-ray spectra of NLS1s (see a review of this topic in Gallo 2018). One of them is the disc reflection model (e.g. Fabian et al. 2004; Larsson et al. 2008; Miniutti et al. 2009; Brenneman et al. 2011; Reis et al. 2012; Tan et al. 2012; Risaliti et al. 2013; Gallo et al. 2013; Walton et al. 2013; Parker et al. 2014a; Marinucci et al. 2014; Jiang et al. 2019b, 2020). The surface of the optically thick disc produces reprocessed emission of the illuminating coronal emission in the soft X-ray band and the Compton-scattering hump in the hard X-ray band. They are often referred to as the disc ‘reflection’ component (Fabian et al. 1989). The most prominent feature of a disc reflection component is the Fe K α emission line around 6.4 keV, which is broadened by relativistic effects in the vicinity of the BH (Tanaka et al. 1995). The disc reflection model of Seyfert active

* E-mail: jcjiang12@outlook.com

galactic nuclei (AGNs) is also supported by the discoveries of X-ray reverberation lags in the soft X-ray band (e.g. [Fabian et al. 2009](#); [De Marco et al. 2013](#)), the Fe K band (e.g. [Kara et al. 2016](#)) and the hard X-ray band (e.g. [Zoghbi et al. 2014](#); [Kara et al. 2015](#)).

Another model used to explain X-ray spectra of Sy1s is the double partially-covering absorption model ([Tanaka et al. 2004](#)). In this model, multiple high-column density absorbers crosses our line of sight towards the X-ray emission region. The absorbers require a tricky geometry to partially cover the compact X-ray emission region as suggested by X-ray data ([Reynolds et al. 2009](#)). In this model, the absorbers produce strong Fe K edge in the spectrum, which is used to explain the steep spectra of some NLS1s (e.g. [Gallo et al. 2015](#)).

An additional component is still required to fit the soft excess emission when one uses the absorption model to fit the data in the Fe K band. For instance, a soft power-law model was used to explain the soft excess emission of the NLS1 1H 0707–495 in combination with the absorption model in [Tanaka et al. \(2004\)](#). Such a soft power-law component is proposed to originate in a warm coronal region with a high optical depth of $\tau_T = 10 - 20$ and a low temperature of $kT_e < 1$ keV ([Magdziarz et al. 1998](#); [Petrucci et al. 2001](#); [Czerny et al. 2003](#); [Jin et al. 2017](#); [Ursini et al. 2020](#)). At such a low temperature, atomic opacity dominates over the Thomson opacity. Strong emission and absorption features could be shown in the spectrum of the warm corona in contradiction to the data of Sy1s ([Garcia et al. 2018](#)). Simulations by [Petrucci et al. \(2020\)](#), however, suggest that the warm corona has to be heated by hard X-ray continuum from the hot corona and the disc emission from below, where the ions in the upper layer of the warm corona can be completely ionised showing no or weak emission and absorption lines. Photoionisation models also find that a higher accretion rate in the accretion disc leads to a warm corona producing stronger soft excess emission, similar to what is suggested by the X-ray data of Sy1s ([Ballantyne 2020](#)).

In this work, we investigate how the models introduced above may explain the *XMM-Newton* observations of the active galaxy UGC 11763 at $z = 0.063$ (23 32 27.8, +10 08 19, [Clements 1981](#); [Huchra et al. 1999](#)). UGC 11763 was classified as a NLS1 galaxy by [Boroson & Green \(1992\)](#); [Constantin & Shields \(2003\)](#). The H β emission of this NLS1 has a width of 2250–2800 km s $^{-1}$ ([Boroson & Green 1992](#); [Grupe et al. 2004a](#); [Mullaney & Ward 2008](#)), which is higher than the values of typical NLS1s. The mass of the central BH in UGC 11763 is estimated to be around $4.57 \times 10^8 M_\odot$ ([Peterson et al. 2004](#)) using broad emission-line reverberation-mapping data. [Ho et al. \(2008\)](#) further lowered this mass measurement by a factor of 1.8 to $2.5 \times 10^8 M_\odot$ for consistency with the virial mass zero point¹ adopted by ([Greene & Ho 2005](#)). These measurements are near the upper limit of the BH mass distribution of NLS1s ([Grupe et al. 2004a](#)). [Peterson et al. \(2004\)](#) estimated the luminosity of UGC 11763 at 5100Å to be $\log(\lambda L_\lambda) = 44.46 \pm 0.04$. Assuming $L_{\text{Bol}} = 9\lambda L_\lambda$ ([Kaspi et al. 2000](#)) and a BH mass of $4.6 \times 10^8 M_\odot$ ([Peterson et al. 2004](#)), the Eddington ratio of UGC 11763 is around 5%.

In the X-ray band, [Cardaci et al. \(2009\)](#) reported a steep X-ray emission from UGC 11763 and strong soft excess emission as well as the *EXOSAT* data of the same source ([Singh et al. 1991](#)). [Cardaci et al. \(2009\)](#) also found Fe ‘Unresolved Transition Array’ (UTA) absorption in the soft X-ray band of UGC 11763, which indicates the existence of photoionised absorbers, e.g. warm absorption

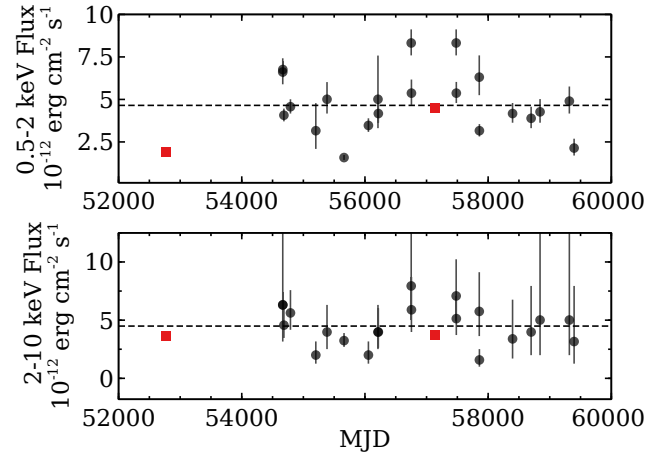


Figure 1. Long-term X-ray lightcurves of UGC 11763 in units of 10^{-12} erg cm $^{-2}$ s $^{-1}$ (top: 0.5–2 keV; bottom: 2–10 keV; black circles: *Swift* XRT observed flux; red squares: *XMM-Newton* pn observed flux). The error bars of the red squares are smaller than the sizes of points. The dashed lines show the average flux of UGC 11763 in the two energy bands.

commonly seen in AGNs (e.g. [Reynolds 1997](#); [George et al. 1998](#)). Large-amplitude X-ray variability of UGC 11763 has been realised for decades and was first discovered by [Singh et al. \(1991\)](#); [Grupe et al. \(2001\)](#). For instance, the X-ray flux of this source measured by *ROSAT* varies by 50% in the 0.1–2 keV band in only one year.

In this paper, we present spectral analysis of the *XMM-Newton* data of UGC 11763 using two archival observations. We consider both the reflection-based and the absorption-based model. In Section 2, we introduce our data reduction processes; in Section 4, we present three models for the spectra of UGC 11763; in Section 5, we discuss our results; in Section 6, we conclude our work.

2 DATA REDUCTION

We use the European Photon Imaging Camera (EPIC) observations for X-ray continuum modelling. A full list of observations used in our work is in Table 1.

The EPIC data are reduced using V20.0 of the *XMM-Newton* Science Analysis System (SAS) software package. The version of the calibration files is v.20220407. We first generate a clean event file by running EMPROC (for EPIC-MOS data) and EP-PROC (for EPIC-pn data). Then, we select good time intervals by filtering out the intervals that are dominated by flaring particle background. These high-background intervals are where the single event (PATTERN=0) count rate in the >10 keV band is larger than 0.35 counts s $^{-1}$ (0.4 counts s $^{-1}$) for MOS (pn) data. By running the EVSELECT task, we select single and double events for EPIC-MOS (PATTERN<=12) and EPIC-pn (PATTERN<=4, FLAG==0) source event lists from a circular source region of 35 arcsec. Background spectra are extracted from a nearby circular region of 60 arcsec. No obvious evidence of pile-up effects has been found in obs1 in 2003. The pn and MOS instruments were operated in the full frame mode in 2015. Some evidence of pile-up effects were found. An annulus region with an inner radius of 10 arcsec and an outer radius of 35 arcsec is used to extract source spectra. The inner

¹ See Footnote 4 in [Greene & Ho \(2005\)](#).

Table 1. The list of *XMM-Newton* observations analysed in this work. $F_{0.3-3\text{keV}}$ and $F_{3-10\text{keV}}$ are the observed flux of UGC 11763 measured by pn in corresponding energy bands.

Name	Obs ID	Date	Time ks	$\log(F_{0.3-3\text{keV}})$ erg cm ⁻² s ⁻¹	$\log(F_{3-10\text{keV}})$ erg cm ⁻² s ⁻¹
obs1	0150470701	2003-05-16	38	-11.467 ± 0.002	$-11.535^{+0.009}_{-0.007}$
obs2	0744370201	2015-05-01	33	-11.141 ± 0.005	-11.483 ± 0.019

radius is chosen according to the EPATPLOT tool in SAS². Last, we create redistribution matrix files and ancillary response files by running RMFGEN and ARFGEN. In this work, we consider the full 0.3–10 keV band of EPIC data. The spectra are grouped to have a minimum of 20 counts per bin and oversample by a factor of 3.

3 SOFT X-RAY VARIABILITY OF UGC 11763

Fig. 1 shows the long-term X-ray lightcurves of UGC 11763 in the 0.5–2 keV and 2–10 keV bands. In particular, the *XMM-Newton* observations analysed in this work are marked with the red squares in the figure. The X-ray flux of UGC 11763 shows variability on timescales of months and years. For instance, the 0.5–2 keV flux of this source increased from the reported minimum flux of 1.6×10^{-12} erg cm⁻² s⁻¹ in April 2011 to the maximum flux 8.3×10^{-12} erg cm⁻² s⁻¹ in April 2014. X-ray variability with a similar amplitude was realised in previous observations (Singh et al. 1991; Grupe et al. 2001).

In this work, we focus on the *XMM-Newton* observations of this source. The first observation was taken during a low flux state and the second was taken during a higher flux state in the soft X-ray band. In comparison with the soft X-ray band, the 2–10 keV flux of UGC 11763 does not show large amplitude variability. This leads to the question—what may cause the X-ray variability of UGC 11763 confined below 2 keV.

We show EPIC-pn lightcurves extracted from the two *XMM-Newton* observations in Fig. 2. Unlike other extreme NLS1s (e.g. McHardy et al. 1995; Boller et al. 2003; Smith & Vaughan 2007; Jin et al. 2017; Alston et al. 2019), UGC 11763 does not show rapid and large-amplitude variability on timescales of kiloseconds in the X-ray band. The lack of rapid variability on kilosecond timescales and the evidence of large-amplitude variability on longer timescales might be related to the relatively higher BH mass of UGC 11763 (a few times $10^8 M_{\odot}$, Peterson et al. 2004; Ho et al. 2008) in comparison with other NLS1s.

4 SPECTRAL ANALYSIS

We use the XSPEC software (v.12.12.1) for spectral analysis (Arnaud 1996). We start our analysis by fitting the spectra above 2 keV with an absorbed power law. The tbnew model is used to account for Galactic absorption (Wilms et al. 2000), which is estimated to

² We use EPATPLOT to estimate the full-band observed-to-model ratios for single and double events based on expected pattern distribution functions from the latest calibration data. This ratio is 0.96 ± 0.01 for singles and 1.12 ± 0.02 for doubles when a circular region is used to extract source products from the pn observation, suggesting evidence of pile-up. Singles and doubles ratios are respectively 0.99 ± 0.02 and 1.03 ± 0.04 when an annulus region with an inner radius of 10 arcsec is used. Similar conclusions are found for MOS observations.

be $N_{\text{H}} = 4.6 \times 10^{20}$ cm⁻² (Willingale et al. 2013). Corresponding data/model ratio plots are shown in Fig. 3. A zoom-in of the 3–10 keV band is shown in the lower panel. Both epochs show evidence of Fe K α emission in the Fe K band. Meanwhile, two epochs show different spectral shape in the soft X-ray band.

In the rest of the section, we focus on modelling the spectra of UGC 11763 using the absorption, disc reflection and hybrid models.

4.1 Relativistic Disc Reflection Model (Model 1)

4.1.1 Model set-up

In the disc reflection scenario, the soft excess is interpreted as part of the reprocessed emission from the inner accretion disc (e.g. Crummy et al. 2006; Jiang et al. 2020). To model the disc reflection component, we use the relxilld model (Model 1, García et al. 2016). A broken power-law emissivity profile parameterised by q1, q2 and R_{b} is considered. Other free parameters include the spin of the BH, the inclination angle, the iron abundance and the electron number density of the disc. The reflection fraction parameter of relxilld is set to be a free, positive number, so the model returns both the hot coronal emission and the corresponding disc reflection spectrum.

By applying relxilld to obs1, we find evidence of absorption features at 0.8 keV. See Fig. 4 for corresponding data/model ratio plots. The goodness of this fit is $\chi^2/\nu = 551.62/424$. The absorption features correspond to Fe UTA, suggesting the existence of photoionised absorbers in a low ionisation state, e.g. warm absorbers commonly seen in AGNs (e.g. Lee et al. 2001; Ebrero et al. 2016). Cardaci et al. (2009) pointed out similar residuals in the spectra of UGC 11763 extracted from obs1 when applying a simple model including Galactic absorption, a power law, a black body and Fe K α emission line.

To fit the absorption features, we use a tabulated version of the xabs photoionised absorption model (Steenbrugge et al. 2003) from SPEX (Kaastra et al. 1996), implemented as an XSPEC table model by Parker et al. (2019) and available from www.michaelparker.space/xspec_models. The version used here assumes the photoionisation is driven by a $\Gamma = 2$ power-law input spectrum, and covers ionisations from $\log(\xi) = -4$ to 5, with parameters for the column density, velocity broadening, and covering fraction.

When fitting the warm absorption features in the data, we assume low velocity broadening of 100 km s⁻¹ and a full-covering geometry. The assumption for this geometry is based on the long distance between warm absorbers and the X-ray emission region: typical warm absorbers are estimated to be near the broad line region (e.g. Reynolds & Fabian 1995).

By including the xabs model, the fit is significantly improved, e.g. $\Delta\chi^2 = 45$ and two more free parameters. We, therefore, conclude that our best-fit model is tbnew * xabs * relxilld (Model 1). We only obtain an upper limit of the Galactic col-

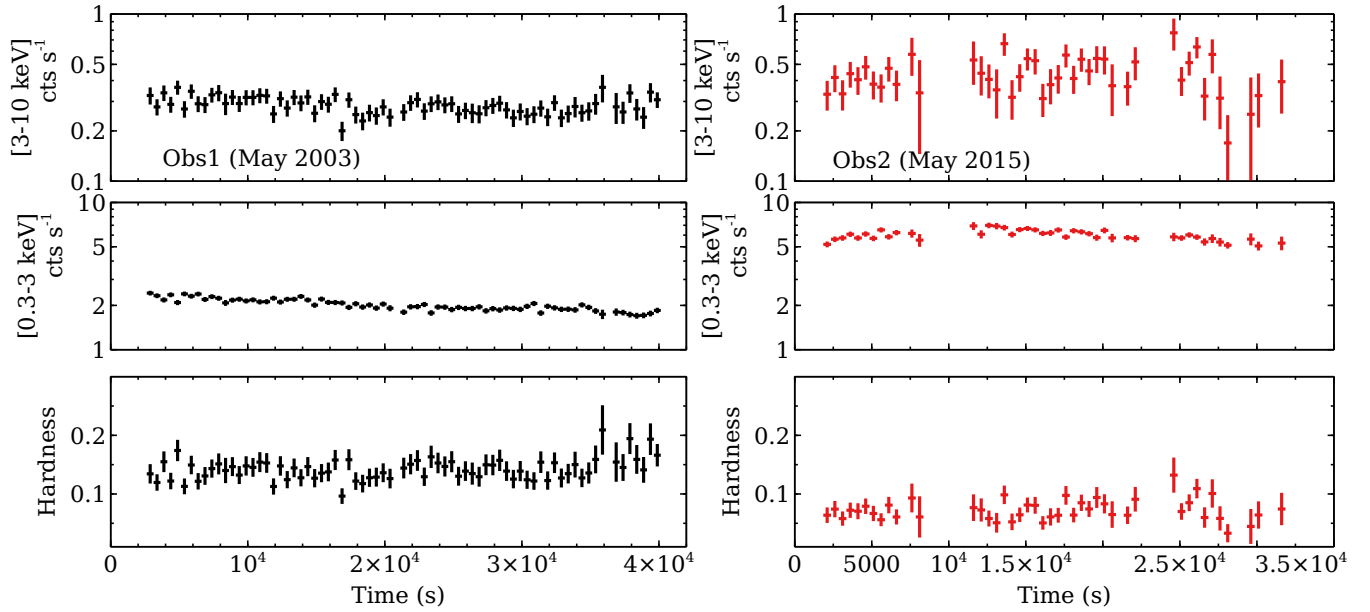


Figure 2. *XMM-Newton* pn lightcurves of UGC 11763 in the 3–10 keV and 0.3–3 keV bands (left: obs1; right: obs2). Note that the y-axes are in log scale. The bottom panels show the hardness ratio defined as the count rate ratio between 3–10 keV and 0.3–3 keV bands. Unlike typical NLS1s, UGC 11763 does not show extreme X-ray variability on timescales of kiloseconds.

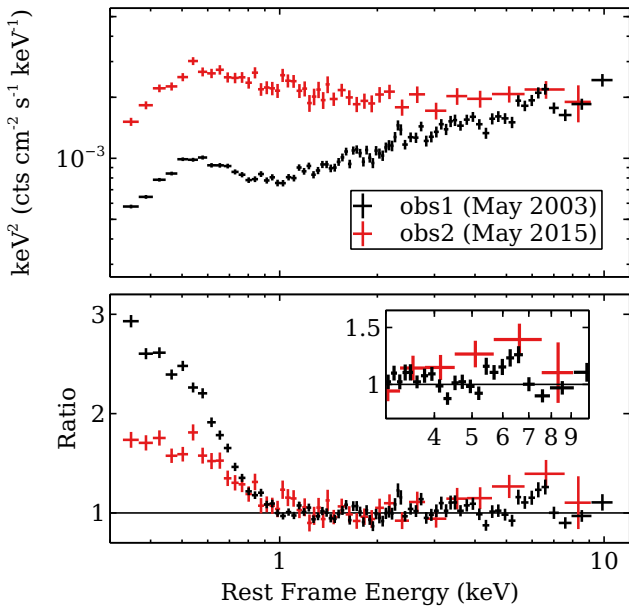


Figure 3. Top: folded EPIC-pn spectra of UGC 11763 corrected for effective area. Two observations, separate by 12 years, show significantly different soft X-ray emission below 1 keV. Bottom: data/model ratio plots of the pn spectra of UGC 11763 using the best-fit absorbed power-law model for the 1–10 keV band of each observation. The smaller panel zooms in on the 4–9 keV band. Both observations show evidence of Fe $K\alpha$ emissions.

umn density ($N_{\text{H}} < 6 \times 10^{20} \text{ cm}^{-2}$). This parameter is thus fixed at the nominal value calculated by Willingale et al. (2013) ($4.6 \times 10^{20} \text{ cm}^{-2}$). Similar conclusions are found for obs2.

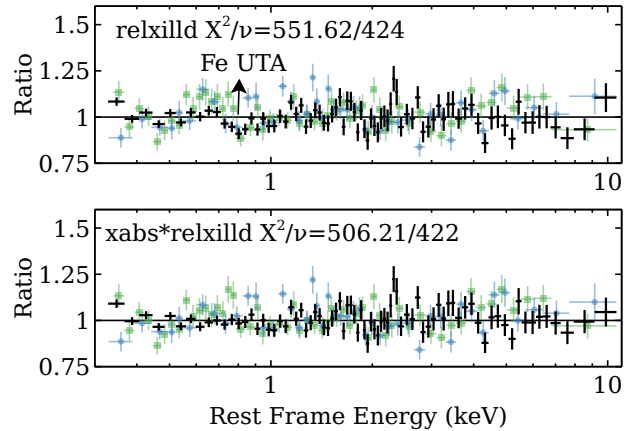


Figure 4. Data/model ratio of the EPIC pn (black), MOS1 (blue crosses) and MOS2 (green squares) spectra of UGC 11763 in 2003 (obs1) using *relxilld* (top). Absorption features at 0.8 keV (16–17 Å) are shown in the data. They are a blend of Fe M-shell absorption lines (Fe ‘Unresolved Transition Array’), suggesting the existence of ionised absorbing gas in UGC 11763. Similar results were found in the grating data of UGC 11763 (Cardaci et al. 2009). An additional low-ionisation absorption model improves the fit by $\Delta\chi^2 = 46$ with two more free parameters (bottom).

4.1.2 Multi-epoch analysis

We fit the two observations of UGC 11763 simultaneously with Model 1 to better understand the spectral variability in this object. Best-fit parameters are shown in the first two columns of Table 2.

Some of the parameters for the two observations are consistent within their uncertainty ranges. For instance, we only obtain an upper limit of the density of the reflection surface of the disk for

each observation. Both values are consistent with a low density of 10^{15} cm^{-3} , which was commonly assumed in the disc reflection modelling of AGN data (e.g. Ross & Fabian 2005). In addition, the spin of the central BH, the inclination angle and iron abundances of the accretion disc are not expected to change on observable timescales. We obtain consistent measurements of these parameters for two observations, which increases our confidence in the choice of our reflection model. Lastly, the ionisation state of the warm absorber also remains consistent in these two observations.

We conduct multi-epoch spectral analysis with all the parameters mentioned above linked between two observations. By doing so, we obtain a good fit for both observations with $\chi^2/\nu = 867.37/721$. The best-fit parameters are shown in Table 2 and the best-fit models are shown in the upper panel of Fig. 5. Corresponding data/model ratio plots are shown in the lower panels of Fig. 5.

4.1.3 Results

By comparing the best-fit parameters of Model 1 for the two *XMM-Newton* observations of UGC 11763, we find that the coronal emission shows a softer-when-brighter pattern—the photon index of the coronal emission increases from 2.26 to 2.41. This is commonly seen in other AGN too (e.g. Jiang et al. 2018; Wu et al. 2020).

The fit of the disc reflection spectrum in obs2 requires a flatter disc emissivity profile, i.e. a lower q_1 and a higher R_b , suggesting a change in the coronal geometry, e.g. a more extended corona in UGC 11763 during obs2 than obs1 (Dauser et al. 2013). The anti-correlation between the X-ray flux and the reflection fraction parameter suggests a similar conclusion. When the coronal region is more compact, more coronal photons are lost to the event horizon. On the other hand, disc reflected photons from a more extended emission region is less affected by light-bending effects, resulting in a higher reflection fraction in the spectrum (e.g. Miniutti et al. 2003).

In summary, the spectral difference between obs1 and obs2 is explained by the variable coronal emission in Model 1. The disc reflection component changes accordingly. During the low flux state (obs1), the coronal region is more compact as suggested by the steeper emissivity profile and the higher reflection fraction parameter. Meanwhile, the variable column density of the warm absorber also contributes to the soft X-ray variability while the ionisation state of the warm absorber remains consistent.

The spin of the BH, the inclination angle of the inner disc and the iron abundances of the disc are not expected to change on observable timescales. By linking these parameters of two observations, we obtain $i = 32 \pm 2^\circ$, $a_* > 0.97$ and $Z_{\text{Fe}} = 4.8 \pm 1.2 Z_\odot$.

The best-fit Model 1 of UGC 11763 suggests that the column density of the warm absorber decreases from $2.5 \pm 0.4 \times 10^{21} \text{ cm}^{-3}$ in obs1 to $1.0 \pm 0.3 \times 10^{21} \text{ cm}^{-3}$ in obs2 while its ionisation state remains consistent. We investigate whether it is possible to explain the X-ray spectral variability of UGC 11763 by varying only the intrinsic continuum emission. By linking the column density parameters of two observations, the fit is significant worse below 1 keV with $\chi^2/\nu = 910.63/723$. Therefore, although the X-ray variability is dominated by the variable intrinsic continuum emission in Model 1, the contribution of the variable line-of-sight column density of the warm absorber in UGC 11763 cannot be ignored.

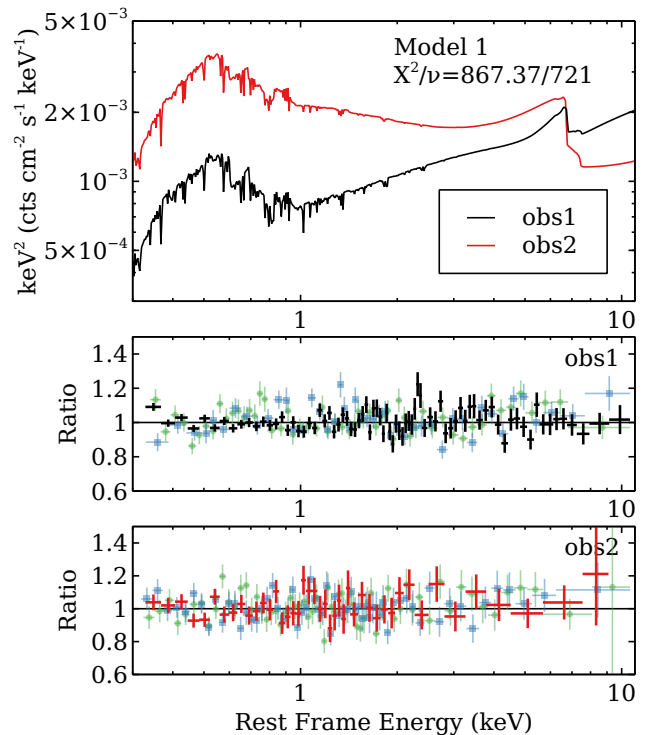


Figure 5. Best-fit models for two *XMM-Newton* observations using Model 1 and corresponding data/model ratio plots (red: obs1 pn; black: obs2 pn; blue squares: MOS1; green circles: MOS2). Spectra extracted from two observations are fit together. See text for more details.

4.2 Partially-Covering Absorption Model (Model 2)

4.2.1 Model set-Up

In this section, we consider a model based on multiple partially-covering absorbers (e.g. Tanaka et al. 2004). In this model, the residuals between 4–8 keV as shown in Fig. 3 are explained by the Fe K absorption edge of two high- N_{H} absorbers (e.g. Waddell et al. 2019).

We first fit the soft excess emission of UGC 11763 to a soft Comptonisation model, similar to the model for another NLS1 Mrk 335 in Gallo et al. (2015). The `comptt` model (Titarchuk 1994; Marshall et al. 2003) is used for this purpose. The combination of warm and hot corona models provides a fit to the obs1 data, for example, with $\chi^2/\nu = 630.42/430$. See the first panel of Fig. 6 for the corresponding data/model ratio plot. Residuals are seen at 6.4 keV and <1 keV, suggesting the existence of Fe K α emission and low-ionisation absorption.

Similar to the absorption model in Tanaka et al. (2004); Gallo et al. (2015), we consider a low-ionisation partially-covering model to fit the negative residuals at 7 keV and the absorption features below 1 keV. The same `xabs` model as in Model 1 is used to model the photoionisation absorption in the data.

One additional `xabs` component improves the fit by $\Delta\chi^2 = 30$ with three more free parameters (N_{H} , $\log(\xi)$ and f_{cov}). See the second panel of Fig. 6 for the corresponding data/model ratio plot. The fit of Fe UTA at 0.8 keV is improved by adding `xabs`. To further improve the fit below 1 keV, we add a second `xabs` model, which decreases χ^2 by 65 with three more free parameters.

We then add an additional `xillver` model (García & Kallman 2010) with the ionisation parameter fixed at $\log(\xi) = 0$ to

Model	Parameter	Unit	obs1 & 2	
xabs	N_{H}	10^{20} cm^{-2}	25 ± 4	7 ± 3
	$\log(\xi)$	erg cm s^{-1}	1.7 ± 0.2	
relxilld	q1	-	8.0 ± 0.3	4.0 ± 0.4
	q2	-	2.9 ± 0.2	$3.1^{+0.7}_{-0.6}$
	R_{b}	r_{g}	$3.4^{+0.2}_{-0.4}$	5 ± 2
	a_*	-	>0.97	
	i	deg	32 ± 2	
	Z_{Fe}	Z_{\odot}	4.8 ± 1.2	
	$\log(n_{\text{e}})$	cm^{-3}	< 15.7	
	$\log(\xi)$	erg cm s^{-1}	1.20 ± 0.15	$1.3^{+0.3}_{-0.2}$
	Γ	-	2.26 ± 0.02	2.49 ± 0.06
	f_{refl}	-	10 ± 4	3.0 ± 1.5
	$\log(F_{\text{X}})$	$\text{erg cm}^{-2} \text{ s}^{-1}$	-11.105 ± 0.008	-10.865 ± 0.015
χ^2/ν		-	$867.37/721$	

Table 2. Best-fit parameters obtained by using Model 1. F_{X} is the unabsorbed flux of the model in the 0.3–10 keV band.

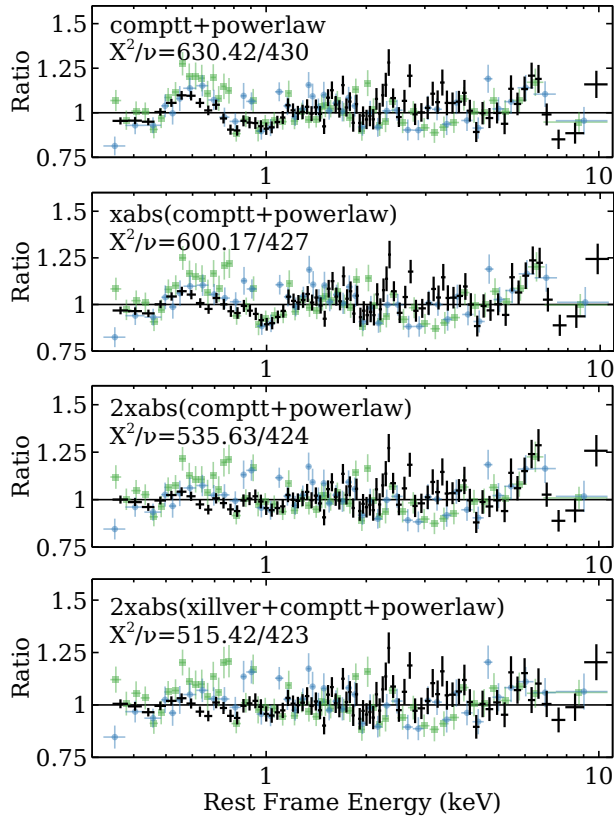


Figure 6. Data/model ratio plots of the obs1 spectra of UGC 11763 fit to different models (red: pn; blue squares: MOS1; green circles: MOS2). See text for more details.

account for narrow Fe $K\alpha$ emission from a distant reflector. The additional reflection component improves the fit by $\Delta\chi^2 = 20$ with one more free parameter. The final best-fit model is `tbnew * xabs1 * xabs2 * (comptt + powerlaw + xillver)` (Model 2) in XSPEC notations. Similar conclusions are found for obs2. In summary, Model 2 needs two layers of low-ionisation absorption in combination with the warm corona model.

Note that some positive residuals are still seen at 6 keV of obs1 using Model 2 (see the last panel of Fig. 6). The combination of narrow Fe $K\alpha$ emission from the distant reflection model and the Fe K absorption from partially-covering absorbers is unable to fit the spectra in the iron emission band perfectly. Relativistic correction for the reflection component is still required, although Model 2 is able to provide an acceptable fit to the X-ray continuum emission of UGC 11763. In Section 4.3, we will further improve the fit in the iron emission band by considering a hybrid model including both absorption and disc reflection.

Lastly, Model 1 offers obs1 a better fit than Model 2 with $\Delta\chi^2 = 9$. The difference of two fits are in not only the iron emission band as described above but also the 8–10 keV band in the observed frame. Positive residuals are seen when fitting the spectra of obs1 with Model 2. In comparison, Model 1 fits the spectra better near the upper limit of the EPIC energy range. Future hard X-ray observations, e.g. from *NuSTAR* (Harrison et al. 2013) or *HEX-P* (Madsen et al. 2019), may help distinguishing two models in the >10 keV band.

4.2.2 Multi-epoch analysis

By applying Model 2 to two observations, we also obtain reasonably good fits for the continuum emission. The best-fit parameters are shown in Table 3. By doing so, we find a good fit for both observations with $\chi^2/\nu = 880.46/721$. Best-fit parameters are shown in Table 3 and the best-fit models are shown in the upper panel of Fig. 7. Corresponding data/model ratio plots are shown in the lower panels of Fig. 7.

In Model 2, the ionisation states of the two absorbers are consistent in two epochs: the first absorber has an ionisation state of $\log(\xi) \approx 2.5$; the second absorber has an ionisation state of $\log(\xi) \approx 0.7$. The covering factor of the first absorber decreases from 0.5 during obs1 to 0.3 during obs2; the same parameter of the second absorber decreases from 0.76 during obs1 to 0.6 during obs2. Furthermore, the optical depth of the warm corona remains consistent with 20 while its temperature increases from 0.15 keV to 0.26 keV.

4.2.3 Results

In Model 2, the soft X-ray variability of UGC 11763 is explained by variable line-of-sight absorption and intrinsic continuum emission including the soft excess emission and the hot coronal emission.

Two partially-covering absorbers in a low-ionisation state, `xabs1` and `xabs2`, are needed in Model 2. The first absorber `xabs1` has a higher column density, a higher ionisation state and a lower covering factor than `xabs2`. For instance, `xabs1` has a column density of $2.8 \times 10^{23} \text{ cm}^{-2}$, which is approximately 18 times the column density of `xabs2`. The ionisation parameter of `xabs1` is around 64 times the same parameter³ of `xabs2`. The covering factor of `xabs1` is lower than that of `xabs2`.

The column density and covering factor of the first absorber `xabs1` increase from the high flux state during `obs2` to the low flux state during `obs1`. The best-fit value of the column density changes by a factor of 3. The covering factor of `xabs1` increases by a factor of 1.6. The column density of the second absorber `xabs2` decreases by a factor of 2 from `obs2` to `obs1` while the covering factor increases by a factor 1.3.

In addition to variable absorption, Model 2 also requires the intrinsic emission to be variable to fit the data. The photon index of the hot coronal emission increases dramatically from 1.8 in `obs1` to 2.5 in `obs2`. The temperature and the strength of the warm corona also increase from `obs1` to `obs2`. In particular, the unabsorbed flux of the warm coronal emission increases by a factor of 13 in the *XMM-Newton* energy band.

We investigate the possibility of fitting the spectra of UGC 11763 using Model 2 without the need of changing the intrinsic emission. The following additional parameters are linked between two epochs: F_w , kT , F_h , Γ and F_x . By doing so, we obtain a worse fit with $\chi^2/\nu = 927.46/726$ than the fit presented in Table 3 and Fig. 7 ($\chi^2/\nu = 880.46/721$). This model requires intermediate values of the parameters for the linked components: for instance, the flux of the warm corona and the hot corona is $\log(F_w) = -11.40^{+0.12}_{-0.19}$ and $\log(F_h) = -10.87^{+0.06}_{-0.07}$; the temperature of the warm corona is $0.21^{+0.03}_{-0.02} \text{ keV}$. Based on the high value of χ^2 of this fit, we argue that Model 2 requires both the intrinsic emission and the absorption to be variable to explain the data.

4.3 Hybrid Model

In previous two sections, we introduce two spectral models to fit the *XMM-Newton* spectra of UGC 11763: one is based on the relativistic disc reflection model (Model 1) and the other is based on double partially-covering absorption model (Model 2). The evidence of Fe $K\alpha$ emission and soft excess in the spectra of UGC 11763 motivates the choice of Model 1. An additional warm absorption model with a modest column density of $1\text{--}2.5 \times 10^{21} \text{ cm}^{-2}$ is required to fit the Fe UTA at 0.8 keV. Alternatively, one may fit the soft excess of UGC 11763 with the warm corona model which is included in Model 2.

In this section, we first compare Model 1 and Model 2 and summarise the interpretations of the soft X-ray variability of UGC 11763 based on two models. We then introduce a hybrid model where the intrinsic emission is described by the relativistic disc reflection model and additional absorption models are used to explain the variability. Such a model can improve the fit in the iron emission and 8–10 keV bands in comparison to Model 2.

³ Note that the ionisation parameter is reported in log in Table 3.

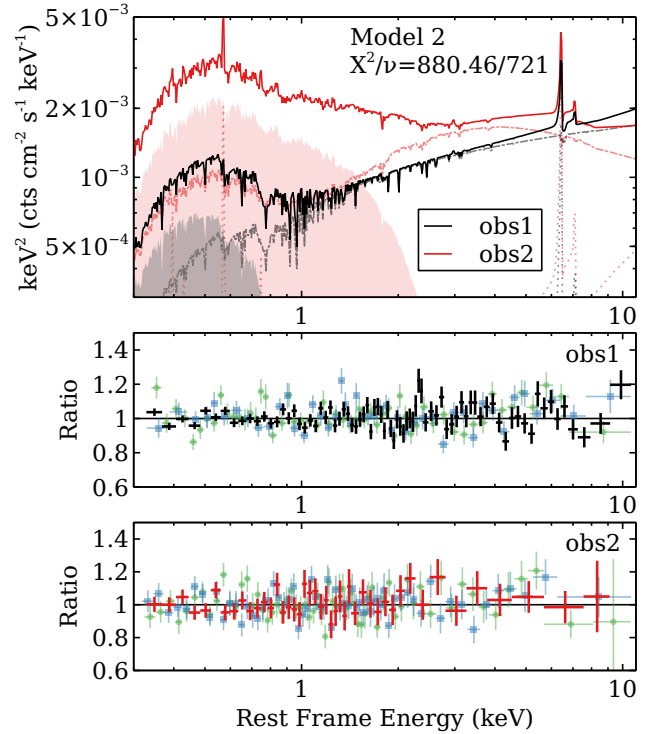


Figure 7. Best-fit models for two *XMM-Newton* observations using Model 2 and corresponding data/model ratio plots (red: `obs1` pn; black: `obs2` pn; blue squares: MOS1; green circles: MOS2). Solid lines: total models; shaded regions: soft Comptonisation models; dash-dotted lines: power-law components; dotted lines: distant reflectors. Spectra of two observations are fit together. See text for more details.

4.3.1 Variable reflection or/and absorption?

UGC 11763 shows significant long-term variability in the $<2 \text{ keV}$ band on timescales of months and years (see Fig. 1). We conduct multi-epoch spectral analysis for the two *XMM-Newton* observations of this object based on Model 1 and Model 2 to study the origin of such variability.

In Model 1, the soft X-ray variability is dominated by the intrinsic emission from the hot corona and the reflected emission from the inner accretion disc. The best-fit unabsorbed Model 1 for two *XMM-Newton* observations is shown in the top panel of Fig. 8. The X-ray continuum emission is softer during `obs2` when the flux is high. The variable disc emissivity profile and reflection fraction of the disc reflection model agrees with the light-bending model (Miniutti et al. 2003), where the size of the coronal region plays an important role. Variability in the column density of the warm absorption, which shows a consistent ionisation state, contribute to the soft X-ray variability too.

In Model 2, both absorption and intrinsic emission contribute to the soft X-ray variability of UGC 11763. Two low-ionisation partially-covering absorbers are required to fit the broad band spectra. They show a higher covering factor when the observed soft X-ray flux of UGC 11763 is low during `obs1`. Meanwhile, they remain consistent ionisation states. The unabsorbed intrinsic emission of Model 2 is shown in the lower panel of Fig. 8. Emission from both hot and warm corona changes: the hot coronal emission becomes softer and the temperature and strength of the warm corona increase. In comparison with Model 1, Model 2 requires the photon

Model	Parameter	Unit	obs1 & obs2	
xabs1	N_{H}	10^{22} cm^{-2}	28_{-6}^{+9}	10 ± 7
	$\log(\xi)$	erg cm s^{-1}	2.5 ± 0.2	
	f_{cov}	-	0.50 ± 0.04	$0.31_{-0.11}^{+0.17}$
xabs2	N_{H}	10^{22} cm^{-2}	1.6 ± 0.3	$3.4_{-0.2}^{+0.7}$
	$\log(\xi)$	erg cm s^{-1}	0.7 ± 0.2	
	f_{cov}	-	0.76 ± 0.04	0.60 ± 0.05
comptt	τ	-	20 ± 3	
	kT	keV	$0.145_{-0.012}^{+0.015}$	0.26 ± 0.02
powerlaw	$\log(F_{\text{w}})$	$\text{erg cm}^{-2} \text{ s}^{-1}$	-11.72 ± 0.02	$-10.6_{-0.4}^{+0.3}$
	Γ	-	1.81 ± 0.07	$2.50_{-0.15}^{+0.13}$
	$\log(F_{\text{h}})$	$\text{erg cm}^{-2} \text{ s}^{-1}$	$-11.16_{-0.02}^{+0.03}$	$-10.72_{-0.12}^{+0.26}$
xillver	$\log(F_{\text{x}})$	$\text{erg cm}^{-2} \text{ s}^{-1}$	$-12.49_{-0.12}^{+0.15}$	-11.8 ± 0.3
χ^2/ν		-	880.46/721	

Table 3. Best-fit parameters obtained by using Model 2.

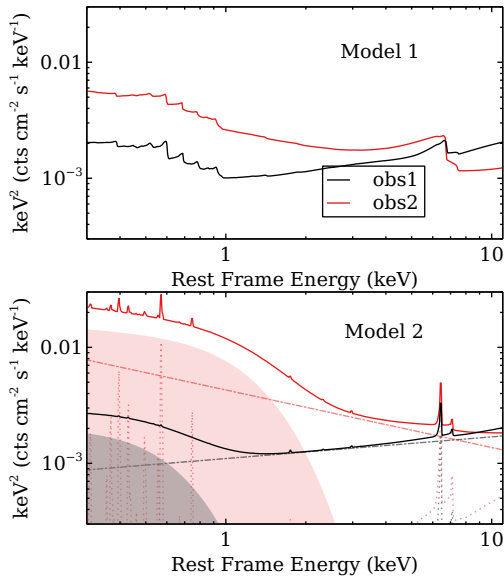


Figure 8. The unabsorbed intrinsic X-ray emission from UGC 11763 during obs1 (black solid lines) and obs2 (red solid lines) suggested by Model 1 (top) and Model 2 (bottom). All low-ionisation absorption in the AGN and Galactic absorption in the foreground are removed in this figure. Dash-dotted lines: hot coronal emission; shaded regions: warm coronal emission; dotted lines: distant reflection components.

index of the hot coronal emission to increase by a larger amplitude: Γ in Model 1 increases from 2.26 in obs1 to 2.49 in obs2; Γ in Model 2 increases from 1.81 to 2.50.

Furthermore, Model 1 provides a slightly better fit to the spectra of two observations than Model 2 by $\Delta\chi^2 = 13$ with the same number of parameters. The difference in the goodness of their fits is in the 6–10 keV band, where the Fe K emission line is not well fit by Model 2 and some positive residuals are still seen above 8 keV (see Fig. 6 and 4).

In addition to Model 2 and Model 1, we propose a hybrid model where the disc reflection model is used to fit the intrinsic emission and absorption models are still needed to explain the variability. Such a model can improve the fit in the 6–10 keV band by modelling the broad Fe $K\alpha$ emission with a relativistic disc model. We

also investigate whether the spectral variability can be explained by variable absorption and power-law emission without the need for changes in the size of the corona in this hybrid model.

4.3.2 Model set-up

In this section, we present a multi-epoch analysis of the *XMM-Newton* spectra of UGC 11763 based on a hybrid model. The relativistic disc reflection model *relxilld* is used to model the intrinsic emission. The same model is used in Section 4.1.2. Two *xabs* models as in Section 4.2.2 are included to account for absorption.

In Model 1, one *xabs* model is included to fit the Fe UTA of the full-covering warm absorber in UGC 11763. Although the variability is dominated by the varying intrinsic emission, the variable column density of the warm absorber cannot be ignored (see Section 4.1.2). In particular, Model 1 also suggests that the size of the coronal region has to change to explain the variable disc emissivity profiles and reflection fractions. In this hybrid model, we study whether it is possible to keep the geometry of the coronal region consistent and interpret the soft X-ray variability with absorption together with changes in the illuminating coronal emission.

To achieve the goals above, we link most of the parameters in *relxilld* between two observations. They include the emissivity profile, density, ionisation and reflection fraction of the disc. Besides, the spin of the central BH, the inclination angle and iron abundances of the disc are not expected to change on observable timescales. So, they are linked too. We try to fit the data with linked photon index, but the fit is significantly worse. We, therefore, allow the photon index and normalisation of *relxilld* to be different in two observations. These two parameters describe the illuminating spectrum of the disc.

The first absorption model *xabs1* is required to fit the spectrum of obs1 but not necessary for obs2 when flux is high. We, therefore, link the column density and ionisation parameter of *xabs1* for two observations. Only an upper limit of the covering factor is found for obs2 ($f_{\text{cov}} < 0.09$). The second absorption model *xabs2* remains a consistent ionisation state. The ionisation parameter is thus linked too. We obtain only a lower limit of the covering factor for *xabs2* at 0.97, suggesting a full-covering geometry. The best-fit ionisation parameter is around 0.9, which is lower than the value of Model 1 but still consistent with typical values in most AGN (Reynolds & Fabian 1995; Laha et al. 2014). Similar to Model 1, the column

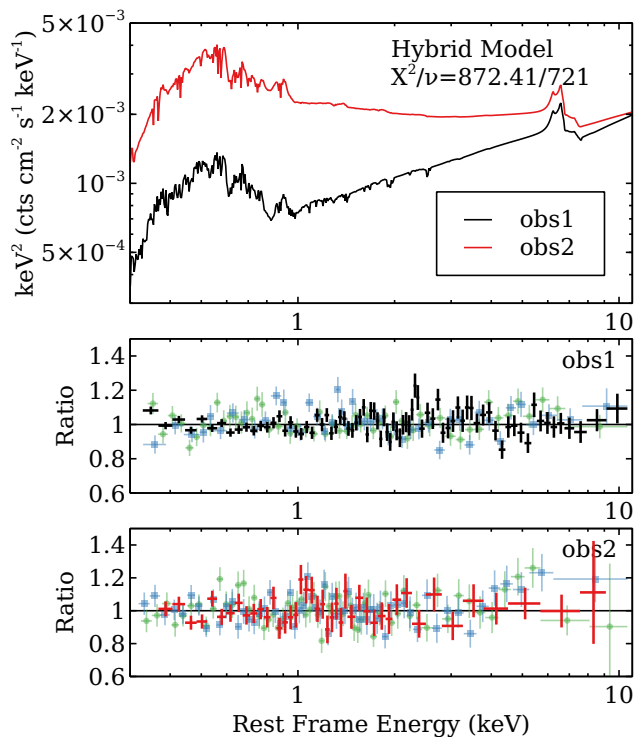


Figure 9. Best-fit models for two *XMM-Newton* observations using a hybrid model and corresponding data/model ratio plots (red: obs1 pn; black: obs2 pn; blue squares: MOS1; green circles: MOS2). Spectra of two observations are fit together. In this scenario, the intrinsic emission is modelled by the relativistic disc reflection model. We assume that the geometry of the coronal region remains consistent. Variable absorption and primary emission from the corona are responsible for the spectral variability.

density of *xabs2* increases from $6 \times 10^{20} \text{ cm}^{-2}$ during the high flux state (obs2) to $1.1 \times 10^{21} \text{ cm}^{-2}$ during the low flux state (obs1).

4.3.3 Results

The hybrid model introduced above provides a good fit to both observations with $\chi^2/\nu = 872.41/721$. The fit is slightly worse than Model 1 by $\Delta\chi^2 = 5$ with the same number of free parameters, and better than Model 2 by $\Delta\chi^2 = 8$ also with the same number of parameters. Best-fit models are shown in Fig. 9 and best-fit parameters are shown in Table 4. The fit in the iron emission band is improved compared to Model 2. Some residuals are still seen above 8 keV in obs1 but reduced from the fit of Model 2.

Assuming the geometry of the coronal region remains consistent, we obtain an intermediate value of reflection fraction for the disc (3.2 ± 0.3), which lies between the values for two observations inferred by Model 1. Similar conclusion is found for the emissivity profile of the disc, which is flatter than the one for obs1 in Model 1 but steeper than the one for obs2. Consistent measurements for the spin of the BH, the inclination and iron abundances of the disc are achieved. Tentative evidence shows that a higher disc density is required when fitting two spectra with the same reflection model. The 90% confidence range of the density parameter is

$\log(n_e/\text{cm}^{-3}) = 16.6^{+0.8}_{-1.0}$. Considering a $3\text{-}\sigma$ uncertainty range⁴, we obtain only an upper limit at 10^{18} cm^{-3} .

In this hybrid model, the strength and shape of the coronal emission are allowed to be different in two epochs. The resulting reflection spectrum changes accordingly with a consistent flux fraction. We show the best-fit unabsorbed models in Fig. 10. The intrinsic emission is softer during obs2 than obs1. The photon index of the power-law emission increases from 2.29 to 2.51. The unabsorbed flux of the *relxilld*, however, does not change a lot ($\log(F) = -11.01$ in obs1 and $\log(F) = -10.82$ in obs2).

Additional variable absorption is needed in the hybrid model. The first absorber *xabs1* is in a higher ionisation state than the second absorber *xabs2*. *xabs1* has a covering factor of 0.47 during obs1 when the soft X-ray flux of UGC 11763 is low. During the high flux state, obs2 requires no *xabs1*. We estimate the upper limit of its covering factor to be at 0.09. The second absorber is similar to typical warm absorbers seen in other AGN. The covering factor is consistent with 1 (>0.97). The column density of *xabs2* decreases by a factor of 2 from obs1 to obs2.

In summary, the hybrid model is also able to explain the multi-epoch variability of UGC 11763. This model provides a slightly worse fit than Model 1 but a better fit than Model 2 with improvements of fitting the data in the 6–10 keV band. In this hybrid model, the soft X-ray variability of UGC 11763 is explained by variable power-law emission from the corona. The reflected emission from the accretion disc changes accordingly without changing the geometry of the corona. During the low flux state, a partially-covering absorber of $\log(\xi) = 1.5$ crosses our line of sight to the source with a covering factor of around 47%. During the high soft X-ray flux state, this absorber moves out of our line of sight. Additional full-covering warm absorber similar to those in other AGN is needed to fit the data. The warm absorber shows a slightly higher column density in obs1 than obs2.

The hybrid model improves the fit in the iron emission band compared to Model 2 by including the relativistic disc reflection model. No additional component is required to fit the soft excess emission. We investigate whether an additional soft Comptonisation component as in Model 2 is able to further improve the fit. The *comptt* model is used for this purpose. We find that the fit is not significantly improved as the disc reflection component accounts for both the iron emission and the soft excess of UGC 11763. We fix the parameters of the *comptt* model at the best-fit values in Model 2 (see Table 3) and then obtain an upper limit for the contribution of the soft Comptonisation component in the 0.3–10 keV band, $F_w < 1.6 \times 10^{-13} \text{ erg cm}^{-2} \text{ s}^{-1}$ and $< 4 \times 10^{-13} \text{ erg cm}^{-2} \text{ s}^{-1}$ respectively for obs1 and obs2.

5 DISCUSSION

We present different spectral models for the *XMM-Newton* observations of UGC 11763. The first model is based on the relativistic disc reflection model and requires a variable size in the coronal region to explain the data. The second model is based on multiple partially-covering absorbers in combination with the warm corona model. The observed soft X-ray variability is interpreted by variable line-of-sight absorption and soft Comptonisation emission. We also propose a third hybrid model, where both multiple absorption and disc reflection models are included. In this scenario, the size of the

⁴ The hard lower limit of n_e in *relxilld* is 10^{15} cm^{-3} .

Model	Parameter	Unit	obs1 & 2	
xabs1	N_{H}	10^{22} cm^{-2}	$1.7^{+0.7}_{-0.6}$	
	$\log(\xi)$	erg cm s^{-1}	$1.52^{+0.20}_{-0.15}$	
	f_{cov}	-	0.47 ± 0.07	<0.09
xabs2	N_{H}	10^{21} cm^{-2}	$1.1^{+0.2}_{-0.3}$	
	$\log(\xi)$	erg cm s^{-1}	0.9 ± 0.2	
	f_{cov}	-	>0.97	
relxilld	q1	-	$5.6^{+0.4}_{-0.5}$	
	q2	-	2.6 ± 0.6	
	R_{b}	r_{g}	$5.5^{+2.0}_{-1.4}$	
	a_*	-	>0.95	
	i	deg	32 ± 3	
	Z_{Fe}	Z_{\odot}	4 ± 2	
	$\log(n_{\text{e}})$	cm^{-3}	$16.6^{+0.8}_{-1.0}$	
	$\log(\xi)$	erg cm s^{-1}	1.06 ± 0.02	
	Γ	-	2.29 ± 0.02	2.51 ± 0.03
	f_{reff}	-	3.2 ± 0.3	
	$\log(F_{\text{X}})$	$\text{erg cm}^{-2} \text{ s}^{-1}$	-11.01 ± 0.02	$-10.82^{+0.03}_{-0.02}$
	χ^2/ν	-	872.41/721	

Table 4. Best-fit parameters obtained by using a hybrid model. F_{X} is the unabsorbed flux of the model in the 0.3–10 keV band.

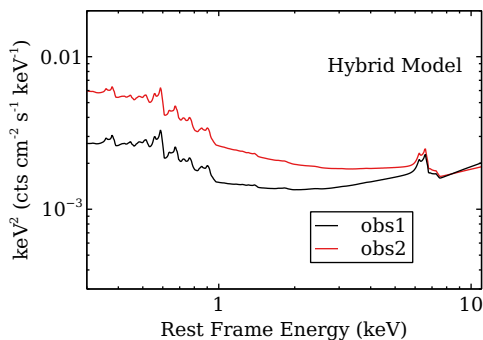


Figure 10. Same as Fig. 8 but for the hybrid model.

corona remains consistent while intrinsic variability in its emission is expected. The soft X-ray variability is dominated by one partially-covering absorber in the low X-ray flux state, which leaves our line of sight during the high X-ray flux state.

5.1 Variable Disc Reflection (Model 1)

In Model 1, the spectral variability is dominated by the Comptonisation emission from the hot corona. The photon index of the coronal continuum emission is higher when the X-ray luminosity is higher, which was often seen in many other Sy1s (e.g. Jiang et al. 2018; Wu et al. 2020).

The resulting disc reflection component changes according to the variable illuminating coronal emission. In particular, the lower flux state observation (obs1) has a higher reflection fraction than the higher flux state observation (obs2). This can be explained by the light-bending effects of the variable size of the corona in UGC 11763 (e.g. Miniutti et al. 2003; Reis et al. 2013; Jiang et al. 2018).

The reflection fraction parameter in relxilld is defined as the ratio between the intensity of the coronal component that reaches the disc and the one seen by the observer, and the value of this pa-

rameter can easily exceed unity when the corona is compact (Dauser et al. 2016). The best-fit reflection fraction parameters for obs1 and obs2 are respectively 10 and 3. Such a large amplitude change of the reflection fraction parameter was also seen in the multi-epoch variability of other AGNs (Jiang et al. 2019a). The high values of reflection fraction parameters suggest that the corona is within a region of $<3 r_{\text{g}}$ assuming a simple ‘lamp-post’ geometry⁵ (Dauser et al. 2016). The flatter disc emissivity profile also suggests the existence of a more extended coronal region in UGC 11763 in obs2 than obs1. Because the outer region of the accretion disc is more illuminated when the coronal region is larger (e.g. Gonzalez et al. 2017). The corona is known to be very compact within a few gravitational radii in many AGN as well as UGC 11763 according to advanced timing analyses in the X-ray band (e.g. Fabian et al. 2009; Reis & Miller 2013). Similar conclusions were found in microlensing events of AGN (Morgan et al. 2008; Chartas et al. 2017). The compact corona also agrees with the predictions of some coronal models, such as magnetic reconnection where the magnetic field increases strength towards smaller radii (Merloni & Fabian 2001), the base of the jet (Ghisellini et al. 2004) and pair productions in the magnetosphere around the central BH (Hirotani & Okamoto 1998; Chen & Yuan 2020).

We estimate the distance of the warm absorber in Model 1 from the central BH using the best-fit ionisation parameter $\xi = 50 \text{ erg cm s}^{-1}$. The bolometric luminosity is estimated to be $9 \times L_{5100} \approx 3.6 \times 10^{45} \text{ erg s}^{-1}$ (Peterson et al. 2004). Assuming a density of $n = 10^9 \text{ cm}^{-3}$ (Reynolds & Fabian 1995) and an isotropic illuminating source, we estimate the location of the warm absorber in UGC 11763 to be around $d = \sqrt{\frac{L_{\text{Bol}}}{4\pi n \xi}} \approx 6 \times 10^{17} \text{ cm}$.

In our calculation, the assumption of $n = 10^9 \text{ cm}^{-3}$ for the warm absorber is based on the agreement of recombination timescale and the variability timescale of the illuminating emission in MCG-6-30-15 (Reynolds & Fabian 1995). If the recombination

⁵ The ‘lamp-post’ model assumes a point-like, isotropic geometry of the corona located on the rotating axis of the BH.

timescale is larger than the variability timescale, photoionization equilibrium would not apply. The primary emission of MCG-6-30-15 is much more variable than UGC 11763 on timescales of kiloseconds. So, the density of the warm absorber in UGC 11763 is allowed to be lower than $n = 10^9 \text{ cm}^{-3}$ as the recombination timescale is approximately proportional to n^{-1} (Reynolds & Fabian 1995). Furthermore, we also assume an isotropic illuminating source and apply a factor of 4π in the calculation, which can also be lower. So, the estimated distance of $6 \times 10^{17} \text{ cm}$ is only the lower limit.

Lastly, Model 1 also provides an estimation of the BH spin of UGC 11763. By fitting two epochs simultaneously and linking their spin parameters, we achieve a high BH spin of $a_* > 0.97$ in Section 4.1.2. Previously, Reynolds (2014) noted the tentative evidence that the most massive black holes ($M_{\text{BH}} > 10^8 M_{\odot}$) and the least massive black holes ($M_{\text{BH}} < 10^6 M_{\odot}$) may have more modest spins by compiling a number of measurements in previous work. The properties of the host galaxy may play an important role in the evolution of the BH spin (Sesana et al. 2014). UGC 11763 may host one of the few massive BHs (Peterson et al. 2004; Ho et al. 2008) which have a high BH spin. Future reflection studies of AGN with similar high BH masses enable us to better understand the spin distribution in a wider range of BH masses.

5.2 Variable Absorption and Intrinsic Soft X-ray Emission (Model 2)

Model 2 provides multi-epoch spectra of UGC 11763 a slightly worse fit than Model 1 by $\Delta\chi^2 = 13$ with the same number of parameters. In Model 2, the ionisation states and the column densities of two absorbers are also consistent within their 90% confidence ranges between two observations. The soft X-ray variability is mainly caused by the variable covering factors of the absorbers: the covering factor of the first absorber increases from 0.34 in obs2 to 0.50 in obs1. We estimate the location of the absorbers according to the X-ray variability assuming the absorbers are orbiting around the central BH: the observed soft X-ray flux of UGC 11763 increases from $\log(F) = -11.47$ in the 0.3–3 keV band in 2003 to $\log(F) = -11.14$ in 2015 (see Table 1) by a factor of more than 2 in 12 years. Meanwhile, the X-ray flux of UGC 11763 does not show large-amplitude variability on kilosecond timescales as many other NLS1s.

We extract long-term lightcurves of UGC 11763 based on *Swift* observations in the archive to investigate how rapidly the soft X-ray emission of UGC 11763 varies. The first two panels of Fig. 1 show the X-ray lightcurves. The X-ray flux of UGC 11763 can amplify by a factor of up to 5 during this long-term period of *Swift* observations. The fifth and sixth *Swift* observations are separated by 6 months in 2010. The soft X-ray flux changes by a factor of 2.7. Similar large-amplitude variability on timescales of months is also seen in other intervals. Assuming a BH mass of $4 \times 10^8 M_{\odot}$, the orbital period at $r = 6.8 \times 10^{13} \text{ m} \approx 100 r_g$ is approximately 6 months. So, if the soft X-ray variability observed by *Swift* results from variable absorption only as inferred by Model 2, the absorbers need to be located less than $\approx 100 r_g$ from the central BH of UGC 11763 to explain the observed large-amplitude X-ray variability on timescales of months.

In addition to the variability in absorption, dramatic changes in the intrinsic emission are also required by Model 2 to explain the spectral variability. The unabsorbed flux of the warm coronal emission increases by a factor of 13 in the *XMM-Newton* energy range. The temperature of the corona increases from 0.18 keV to 0.23 keV.

In the warm corona model, the soft Comptonisation emission

from the warm corona is often found to dominate the extreme-UV band (e.g. Jin et al. 2017). We extend our best-fit models to the extreme-UV band and calculate their predicted flux in the 0.01–0.1 keV band where the soft Comptonisation emission peaks. The warm corona model suggests that the unabsorbed extreme-UV flux of the non-thermal emission in UGC 11763 increase by a factor of 9 from $4 \times 10^{-12} \text{ erg cm}^{-2} \text{ s}^{-1}$ to $3.6 \times 10^{-11} \text{ erg cm}^{-2} \text{ s}^{-1}$. A significant change in the bolometric luminosity is thus expected in Model 2. It is interesting to note that the Eddington ratio of UGC 11763 is estimated to be around 5% based on the observed 5100Å luminosity (see Section 1). The soft excess emission plays an important role in the estimation of bolometric luminosities for AGN at a few percent of Eddington when the warm corona model is used (Noda & Done 2018).

In comparison, the relativistic disc reflection model in Model 1 suggests that the unabsorbed flux of the non-thermal emission in UGC 11763 increases by a factor of only 2.9 from $2 \times 10^{-12} \text{ erg cm}^{-2} \text{ s}^{-1}$ to $5.7 \times 10^{-12} \text{ erg cm}^{-2} \text{ s}^{-1}$ in the 0.01–0.1 keV band. A much smaller increase in the extreme-UV luminosity is required in the disc reflection model. Unfortunately, due to Galactic absorption, it is not possible to measure the luminosity of UGC 11763 in this energy band and test each model.

The Optical Monitor on *XMM-Newton* provides complementary optical and UV views of UGC 11763 at longer wavelengths, although we are unable to measure the extreme-UV flux of this object. The observed magnitude of UGC 11763 increases by a factor of 2 from 13.597 ± 0.008 during obs1 to 13.307 ± 0.007 during obs2 in the UVW1 band and a factor of 2.3 from 13.692 ± 0.008 to 13.337 ± 0.007 in the UVM2 band. Photometric observations with only two filters are not able to constrain the thermal emission from the disc and thus the spectral energy distribution of this object. But we find that the observed UV flux at longer wavelengths varies by a similar factor as the extreme-UV flux predicted by the disc reflection model rather than the warm corona model.

5.3 Hybrid Model

Based on the fits of Model 1 and Model 2, we propose for a hybrid model, where the intrinsic emission is modelled by disc reflection and absorption is still required to explain the spectral variability in UGC 11763. This hybrid model also provides a good fit to the data. Such a model improves the fit in the iron emission band in comparison with the absorption model, Model 2.

In the hybrid model, the variability of the intrinsic X-ray emission from UGC 11763 is caused by the variable intrinsic power-law emission from the corona. The flux of the coronal emission increases by a small amplitude from $9.5 \times 10^{-12} \text{ erg cm}^{-2} \text{ s}^{-1}$ to $1.4 \times 10^{-11} \text{ erg cm}^{-2} \text{ s}^{-1}$ while its photon index increases from 2.29 to 2.51. We assume the coronal region remains the same geometry during the two observations in this model. The resulting disc reflection spectrum changes according to the variable power-law emission with a consistent reflection fraction.

Furthermore, two layers of absorption are needed to explain the spectral variability of UGC 11763: one full-covering warm absorption with a modest column density of approximately 10^{21} cm^{-3} and one partially-covering absorber in a higher ionisation state of $\log(\xi) \approx 1.7$. The partially-covering absorber has a covering factor of 47% in obs1 when the flux is low and disappear on the line of sight during obs2. Assuming this partially-covering absorber contributes to the variability of UGC 11763 on timescales of months observed by *Swift*, this absorber needs to be located in the region of $< 100 r_g$. Variable absorption at a large distance along the line

of sight has been seen in other AGN too (e.g. Grupe et al. 2004b; Parker et al. 2014b; Kaastra et al. 2018; Miller et al. 2021). Objects like NGC 6814 require both disc reflection and absorption models to fit the X-ray data (Gallo et al. 2021). Variable absorption at a large distance from the innermost X-ray emission region plays an important role in the observed variability of these sources.

6 CONCLUSION

In this work, we investigate the nature of the soft X-ray variability of the NLS1 AGN UGC 11763 based on two *XMM-Newton* observations in the archive. The soft excess emission of UGC 11763 shows a very different spectral shape in these two observations. We apply two models to the EPIC data of the source, one based on relativistic disc reflection (Model 1) and the other based on partially-covering absorption in combination with the warm corona model (Model 2).

In the reflection scenario, the X-ray variability of UGC 11763 is dominated by the variable emission from the hot corona. The disc reflection component changes accordingly. The anti-correlation between the reflection fraction parameter and the X-ray flux suggests a variable coronal geometry in UGC 11763. The flatter disc emissivity profile also supports the conclusion that the coronal region of UGC 11763 is more extended during the high X-ray flux state than the low X-ray flux state. The variable modest column density of the line-of-sight warm absorption also contributes to the soft X-ray variability.

In the absorption scenario, the two high- N_{H} absorbers produce strong Fe K edges in the Fe K band. An additional low-ionisation reflection component is required to fit the Fe K α emission of UGC 11763. The variability of UGC 11763 is caused by the variable covering factor of the line-of-sight absorbers in this model, while they remain in a consistent low-ionisation state. *Swift* observations suggest that the absorbers have to be located within a region of $r \approx 100r_g$ to explain the large-amplitude X-ray variability of UGC 11763 on timescales of months. In addition, the intrinsic emission from the AGN also needs to be variable: the temperature and strength of the warm corona increases.

To further improve the fit in the iron band based on Model 2, we investigate the possibility of a hybrid model, where 1) we assume that the geometry of the coronal region remains the same during the two observations; 2) the intrinsic power-law emission from the corona is allowed to vary; 3) variable absorption is used to explain the soft X-ray variability. Such a hybrid model offers a slightly better fit than Model 2. The variable absorbers in the hybrid model have two component, one full-covering warm absorber as those commonly seen in typical AGN (Reynolds & Fabian 1995) and one partially-covering absorber. The partially-covering absorber has a covering factor of 47% during obs1 when the observed soft X-ray flux of UGC 11763 is low and completely moves out of our line of sight during obs2 when the observed flux is high.

Model 1, 2 and the hybrid model provide CCD-resolution data of UGC 11763 with a similarly good fit. However, a different number of absorbers in different ionisation states is needed in them. Unfortunately, archival EPIC data of *XMM-Newton* do not have high enough spectral resolutions to distinguish these models. The RGS observation of obs2 is off-axis. No high-resolution soft X-ray spectrum during obs2 is available for comparison. But future high-resolution X-ray observations, e.g. from *Athena* (Barcons et al. 2017) and *XRISM* (XRISM Science Team 2020), might provide us with a unique opportunity to constrain any of the models for UGC 11763 by resolving multiple spectral components, e.g., from

disc reflection (Parker et al. 2022a) and warm absorption (Parker et al. 2022b).

ACKNOWLEDGEMENTS

This paper was written during the worldwide COVID-19 pandemic in 2022. We acknowledge the hard work of all the health care workers around the world. We would not be able to finish this paper without their protection. J.J. acknowledges support from the Leverhulme Trust, the Isaac Newton Trust and St Edmund's College, University of Cambridge. This work is based on observations obtained with *XMM-Newton*, an ESA science mission with instruments and contributions directly funded by ESA Member States and NASA. This project has made use of the Science Analysis Software (SAS), an extensive suite to process the data collected by the *XMM-Newton* observatory.

DATA AVAILABILITY

All the data can be downloaded from the HEASARC website at <https://heasarc.gsfc.nasa.gov>. The `relxill` package can be downloaded at <https://www.sternwarte.uni-erlangen.de/dauser/research/relxill/index.html>.

REFERENCES

- Alston W. N., et al., 2019, *MNRAS*, **482**, 2088
 Arnaud K. A., 1996, XSPEC: The First Ten Years
 Ballantyne D. R., 2020, *MNRAS*, **491**, 3553
 Barcons X., et al., 2017, *Astronomische Nachrichten*, **338**, 153
 Boller T., Brandt W. N., Fink H., 1996, *A&A*, **305**, 53
 Boller T., Tanaka Y., Fabian A., Brandt W. N., Gallo L., Anabuki N., Haba Y., Vaughan S., 2003, *MNRAS*, **343**, L89
 Boroson T. A., 2002, *ApJ*, **565**, 78
 Boroson T. A., Green R. F., 1992, *ApJS*, **80**, 109
 Brenneman L. W., et al., 2011, *ApJ*, **736**, 103
 Cardaci M. V., Santos-Lleó M., Krongold Y., Hägele G. F., Díaz A. I., Rodríguez-Pascual P., 2009, *A&A*, **505**, 541
 Chartas G., Krawczynski H., Zalesky L., Kochanek C. S., Dai X., Morgan C. W., Mosquera A., 2017, *ApJ*, **837**, 26
 Chen A. Y., Yuan Y., 2020, *The Astrophysical Journal*, **895**, 121
 Clements E. D., 1981, *MNRAS*, **197**, 829
 Constantin A., Shields J. C., 2003, *PASP*, **115**, 592
 Crummy J., Fabian A. C., Gallo L., Ross R. R., 2006, *MNRAS*, **365**, 1067
 Czerny B., Nikołajuk M., Różańska A., Dumont A. M., Loska Z., Zycki P. T., 2003, *A&A*, **412**, 317
 Dauser T., García J., Wilms J., Böck M., Brenneman L. W., Falanga M., Fukumura K., Reynolds C. S., 2013, *MNRAS*, **430**, 1694
 Dauser T., García J., Walton D. J., Eikmann W., Kallman T., McClintock J., Wilms J., 2016, *A&A*, **590**, A76
 De Marco B., Ponti G., Cappi M., Dadina M., Uttley P., Cackett E. M., Fabian A. C., Miniutti G., 2013, *MNRAS*, **431**, 2441
 Ebrero J., et al., 2016, *A&A*, **587**, A129
 Fabian A. C., Rees M. J., Stella L., White N. E., 1989, *MNRAS*, **238**, 729
 Fabian A. C., Miniutti G., Gallo L., Boller T., Tanaka Y., Vaughan S., Ross R. R., 2004, *MNRAS*, **353**, 1071
 Fabian A. C., et al., 2009, *Nature*, **459**, 540
 Gallo L. C., 2006, *MNRAS*, **368**, 479
 Gallo L., 2018, in *Revisiting Narrow-Line Seyfert 1 Galaxies and their Place in the Universe*. p. 34 ([arXiv:1807.09838](https://arxiv.org/abs/1807.09838))
 Gallo L. C., et al., 2013, *MNRAS*, **428**, 1191
 Gallo L. C., et al., 2015, *MNRAS*, **446**, 633
 Gallo L. C., Gonzalez A. G., Miller J. M., 2021, *ApJ*, **908**, L33

- García J., Kallman T. R., 2010, *ApJ*, **718**, 695
- García J. A., Fabian A. C., Kallman T. R., Dauser T., Parker M. L., McClintock J. E., Steiner J. F., Wilms J., 2016, *MNRAS*, **462**, 751
- García J. A., et al., 2018, arXiv e-prints, p. [arXiv:1812.03194](https://arxiv.org/abs/1812.03194)
- George I. M., Turner T. J., Netzer H., Nandra K., Mushotzky R. F., Yaqoob T., 1998, *ApJS*, **114**, 73
- Ghisellini G., Haardt F., Matt G., 2004, *A&A*, **413**, 535
- Gonzalez A. G., Wilkins D. R., Gallo L. C., 2017, *MNRAS*, **472**, 1932
- Goodrich R. W., 1989, *ApJ*, **342**, 224
- Greene J. E., Ho L. C., 2005, *ApJ*, **630**, 122
- Grupe D., Mathur S., 2004, *ApJ*, **606**, L41
- Grupe D., Beuermann K., Thomas H. C., Mannheim K., Fink H. H., 1998, *A&A*, **330**, 25
- Grupe D., Thomas H. C., Beuermann K., 2001, *A&A*, **367**, 470
- Grupe D., Wills B. J., Leighly K. M., Meusinger H., 2004a, *AJ*, **127**, 156
- Grupe D., Leighly K. M., Burwitz V., Predehl P., Mathur S., 2004b, *AJ*, **128**, 1524
- Harrison F. A., et al., 2013, *ApJ*, **770**, 103
- Hirotoni K., Okamoto I., 1998, *The Astrophysical Journal*, **497**, 563
- Ho L. C., Darling J., Greene J. E., 2008, *ApJS*, **177**, 103
- Huchra J. P., Vogeley M. S., Geller M. J., 1999, *ApJS*, **121**, 287
- Jiang J., et al., 2018, *MNRAS*, **477**, 3711
- Jiang J., Walton D. J., Fabian A. C., Parker M. L., 2019a, *MNRAS*, **483**, 2958
- Jiang J., Fabian A. C., Wang J., Walton D. J., García J. A., Parker M. L., Steiner J. F., Tomsick J. A., 2019b, *MNRAS*, **484**, 1972
- Jiang J., Gallo L. C., Fabian A. C., Parker M. L., Reynolds C. S., 2020, *MNRAS*, **498**, 3888
- Jin C., Done C., Ward M., Gardner E., 2017, *MNRAS*, **471**, 706
- Kaastra J. S., Mewe R., Nieuwenhuijzen H., 1996, in *UV and X-ray Spectroscopy of Astrophysical and Laboratory Plasmas*. pp 411–414
- Kaastra J. S., et al., 2018, *A&A*, **619**, A112
- Kara E., et al., 2015, *MNRAS*, **446**, 737
- Kara E., Alston W. N., Fabian A. C., Cackett E. M., Uttley P., Reynolds C. S., Zoghbi A., 2016, *MNRAS*, **462**, 511
- Kaspi S., Smith P. S., Netzer H., Maoz D., Jannuzi B. T., Giveon U., 2000, *ApJ*, **533**, 631
- Laha S., Guainazzi M., Dewangan G. C., Chakravorty S., Kembhavi A. K., 2014, *MNRAS*, **441**, 2613
- Larsson J., Miniutti G., Fabian A. C., Miller J. M., Reynolds C. S., Ponti G., 2008, *MNRAS*, **384**, 1316
- Lee J. C., Ogle P. M., Canizares C. R., Marshall H. L., Schulz N. S., Morales R., Fabian A. C., Iwasawa K., 2001, *ApJ*, **554**, L13
- Madsen K., et al., 2019, in *Bulletin of the American Astronomical Society*. p. 166
- Magdziarz P., Blaes O. M., Zdziarski A. A., Johnson W. N., Smith D. A., 1998, *MNRAS*, **301**, 179
- Marconi A., Axon D. J., Maiolino R., Nagao T., Pastorini G., Pietrini P., Robinson A., Torricelli G., 2008, *ApJ*, **678**, 693
- Marinucci A., et al., 2014, *MNRAS*, **440**, 2347
- Marshall H. L., Edelson R. A., Vaughan S., Malkan M., O’Brien P., Warwick R., 2003, *AJ*, **125**, 459
- McHardy I. M., Green A. R., Done C., Puchnarewicz E. M., Mason K. O., Branduardi-Raymont G., Jones M. H., 1995, *MNRAS*, **273**, 549
- Merloni A., Fabian A. C., 2001, *MNRAS*, **321**, 549
- Miller J. M., et al., 2021, *ApJ*, **911**, L12
- Miniutti G., Fabian A. C., Goyder R., Lasenby A. N., 2003, *MNRAS*, **344**, L22
- Miniutti G., Panessa F., de Rosa A., Fabian A. C., Malizia A., Molina M., Miller J. M., Vaughan S., 2009, *MNRAS*, **398**, 255
- Morgan C. W., Kochanek C. S., Dai X., Morgan N. D., Falco E. E., 2008, *ApJ*, **689**, 755
- Mullaney J. R., Ward M. J., 2008, *MNRAS*, **385**, 53
- Noda H., Done C., 2018, *MNRAS*, **480**, 3898
- Parker M. L., et al., 2014a, *MNRAS*, **443**, 1723
- Parker M. L., Schartel N., Komossa S., Grupe D., Santos-Lleó M., Fabian A. C., Mathur S., 2014b, *MNRAS*, **445**, 1039
- Parker M. L., et al., 2019, *MNRAS*, **483**, L88
- Parker M. L., Matzeu G. A., Matthews J. H., Middleton M. J., Dauser T., Jiang J., Joyce A. M., 2022a, *MNRAS*, **513**, 551
- Parker M. L., Lieu M., Matzeu G. A., 2022b, *MNRAS*, **514**, 4061
- Peterson B. M., et al., 2004, *ApJ*, **613**, 682
- Petrucci P. O., et al., 2001, *ApJ*, **556**, 716
- Petrucci P. O., et al., 2020, *A&A*, **634**, A85
- Piconcelli E., Jimenez-Bailón E., Guainazzi M., Schartel N., Rodríguez-Pascual P. M., Santos-Lleó M., 2005, *A&A*, **432**, 15
- Puchnarewicz E. M., et al., 1992, *MNRAS*, **256**, 589
- Reis R. C., Miller J. M., 2013, *ApJ*, **769**, L7
- Reis R. C., et al., 2012, *ApJ*, **745**, 93
- Reis R. C., Miller J. M., Reynolds M. T., Fabian A. C., Walton D. J., Cackett E., Steiner J. F., 2013, *ApJ*, **763**, 48
- Reynolds C. S., 1997, *MNRAS*, **286**, 513
- Reynolds C. S., 2014, *Space Sci. Rev.*, **183**, 277
- Reynolds C. S., Fabian A. C., 1995, *MNRAS*, **273**, 1167
- Reynolds C. S., Fabian A. C., Brenneman L. W., Miniutti G., Uttley P., Gallo L. C., 2009, *MNRAS*, **397**, L21
- Risaliti G., et al., 2013, *Nature*, **494**, 449
- Ross R. R., Fabian A. C., 2005, *MNRAS*, **358**, 211
- Sesana A., Barausse E., Dotti M., Rossi E. M., 2014, *ApJ*, **794**, 104
- Singh K. P., Rao A. R., Vahia M. N., 1991, *ApJ*, **372**, 49
- Smith R., Vaughan S., 2007, *MNRAS*, **375**, 1479
- Steenbrugge K. C., Kaastra J. S., de Vries C. P., Edelson R., 2003, *A&A*, **402**, 477
- Tan Y., Wang J. X., Shu X. W., Zhou Y., 2012, *ApJ*, **747**, L11
- Tanaka Y., et al., 1995, *Nature*, **375**, 659
- Tanaka Y., Boller T., Gallo L., Keil R., Ueda Y., 2004, *PASJ*, **56**, L9
- Titarchuk L., 1994, *ApJ*, **434**, 570
- Ursini F., et al., 2020, *A&A*, **634**, A92
- Waddell S. G. H., Gallo L. C., Gonzalez A. G., Tripathi S., Zoghbi A., 2019, *MNRAS*, **489**, 5398
- Walton D. J., Nardini E., Fabian A. C., Gallo L. C., Reis R. C., 2013, *MNRAS*, **428**, 2901
- Willingale R., Starling R. L. C., Beardmore A. P., Tanvir N. R., O’Brien P. T., 2013, *MNRAS*, **431**, 394
- Wilms J., Allen A., McCray R., 2000, *ApJ*, **542**, 914
- Wu Y.-J., Wang J.-X., Cai Z.-Y., Kang J.-L., Liu T., Cai Z., 2020, *Science China Physics, Mechanics, and Astronomy*, **63**, 129512
- XRISM Science Team 2020, arXiv e-prints, p. [arXiv:2003.04962](https://arxiv.org/abs/2003.04962)
- Zoghbi A., et al., 2014, *ApJ*, **789**, 56

This paper has been typeset from a $\text{\TeX}/\text{\LaTeX}$ file prepared by the author.